Ocean waves in the South Pacific: complementarity of SWIM and SAR observations

Ludivine Oruba, Danièle Hauser, Serge Planes, Emmanuel Dormy

Accepted for publication in *Earth and Space Science*

Ocean waves in the South Pacific: complementarity of SWIM and SAR observations

L. Oruba[1], D. Hauser[1], S. Planes[2], E. Dormy[3]

[1]Laboratoire Atmosphères Milieux Observations Spatiales (LATMOS/IPSL), Sorbonne Université, UVSQ, CNRS, Paris, France.

[2]CRIOBE/USR 3278, CNRS-EPHE-UPVD, Moorea, Polynésie Française.

[3]Département de Mathématiques et Applications, UMR-8553, École Normale Supérieure, CNRS, PSL University, 75005 Paris, France.

Corresponding author: Emmanuel Dormy (emmanuel.dormy@ens.fr)

Key Points:

- Spaceborne observations of ocean waves from the real-aperture rotating radar SWIM (onboard CFOSAT) are analyzed in coral reef environments of the South Pacific.
- SWIM observations are shown to be very consistent with *in situ* measurements deployed on the outer slope of a coral reef island.
- SWIM and SAR (Sentinel-1) measurements complement each other depending on wavelength, wave height and propagation direction.

Abstract

This study focuses on ocean waves impacting the Moorea Island in French Polynesia, where coral reefs play an essential role in the biodiversity and protection of habitations. We investigate how the innovative SWIM instrument of the CFOSAT satellite enables to document on a multi-annual basis, the spectral properties of ocean waves reaching the coasts of the Moorea Island. Our analysis is based on comparisons with *in situ* measurements (wave gauges deployed on the outer slope of the coral reef), and with other satellite observations (altimeter, SAR). Accounting for local masking effects, we show that SWIM provides relevant information on short swell or wind waves, which is missed by the SAR observations, in particular in high sea-state conditions, owing to the dominant propagation direction being close to the azimuth. We, nevertheless, also find that wave properties in low sea-state conditions are better documented by SAR than by SWIM. Such results are important to accurately measure and predict the wave conditions which fragilize the coral reefs and to evaluate the impact of extreme events on tropical islands and coral reefs.

Plain Language Summary

Tropical islands have to face, because of climate change, both sea level rise and more extreme weather events. Here, focusing on an island in French Polynesia, we investigate sea state reconstruction using satellite measurements and stress the importance of relatively short wavelength (below 150 m) in order to estimate large amplitude ocean waves. We highlight that, in this part of the world, the most recent satellite technologies allow a finer estimate of those large waves. This opens the scope both for finer predictions and a posteriori analysis.

1 Introduction

Coral reefs are biodiverse and productive ecosystems and provide many valuable services to more than 500 million people worldwide (Hoegh-Guldberg et al, 2019). They offer a natural protection to coastal societies by sheltering them from large oceanic waves (Beck et al, 2018). They are however threatened by intensifying anthropogenic disturbances and climate change (Cinner et al, 2018). This study focuses on French Polynesia, where coral reefs are an integral part of the biodiversity and where habitations are mainly built in coastal area protected by coral reefs. Located within the South Pacific Ocean, French Polynesia is affected by numerous huge swell episodes generated by atmospheric depressions that have developed at higher latitudes mainly in the southern Pacific, trade winds and occasionally tropical cyclones (Kuleshov et al, 2008).

Wind-generated waves can be studied using three different approaches: *in situ* measurements, satellite observation and numerical modelling. On the *in situ* side, numerous buoy networks, such as the network of the US National Data Buoy Center, provide local measurements of the wave height, wave directions and wavelengths. Underwater pressure sensors can also be used to obtain coastal measurements of water waves (Bishop & Donelan, 1987). Until 2018, satellite wave measurements consisted of two main techniques: satellite radar altimeters, providing a global coverage of significant wave height (SWH) (e.g. Ribal & Young, 2019), and Synthetic Aperture Radars (SAR) giving access to two-dimensional wave spectra (e.g. missions SEASAT, ERS, ENVISAT, Radarsat and Sentinel-1 since 2014). Numerical models have also been developed since the 70's in order to investigate and predict ocean waves (e.g. Cavaleri et al, 2007). These include the so-called third-generation wave models, such as WAVEWATCH III (Tolman, 1998), the WAve Model WAM (WAMDI Group, 1998) or the coastal model Simulating WAves Nearshore (SWAN) (Booij et al, 1999). Here, we use the French version of the WAM model used by the French weather forecast agency (Météo-France) to provide forecasts for the global ocean sea surface waves, the so called Météo France WAve Model (MFWAM). The accuracy of such forecasts is highly dependent on that of the surface wind which acts as a forcing term in these models. The amount and the quality of *in situ* and satellite wave measurements, used in numerical models through data assimilation methods, play also an important role in the forecast accuracy.

Since 2019, the Chinese-French Oceanography SATellite (CFOSAT) has been the first satellite to provide wave measurements thanks to a rotating multi-beam radar, known as the Surface Waves Investigation and Monitoring (SWIM) instrument (Hauser et al, 2017; Hauser et al, 2021). The SWIM wave measurements have already proven useful to improve ocean wave forecast. Aouf et al (2021), for example, have recently shown that the assimilation of SWIM spectra in the MFWAM model allows more accurate predictions of wave growth in the Southern Ocean. SWIM provides wave properties in the wavelength range [70–500 m]. This, so far uncovered range, allows to describe both the wind sea and the swell waves. The former is strongly

correlated to the local wind field whereas the latter is not, because it propagates away from the generation area. So far, SAR instruments were providing the most reliable satellite spectral wave measurements, although they are limited by the so-called azimuth cut-off. This azimuth cut-off results from the non-linear velocity bunching effect in the SAR image formation, which increases with wind-speed and wave height. When waves propagate in the along-track direction, only waves with wavelengths longer than the cut-off can be detected. It roughly varies between 100 m and 500 m. Such a large value being reached when surface winds become larger than about 20 m/s (Alpers & Brüning, 1986; Kerbaol et al, 1998; Hasselmann et al, 2012). For waves propagating away from the azimuth direction, the shortest detectable wavelength is the product of the azimuth cut-off wavelength and of the cosine of the angle between waves and the satellite along-track direction (SAR azimuth direction); the finest resolution being in the range direction (90° away from the azimuth) and corresponding to the range cut-off wavelength. This effect inherent to SAR technology happens to prevent measurements of short swell and wind sea component of ocean waves when they propagate in a direction close to the azimuth. A direct consequence is an underestimation of the waves parameters, among which the significant wave height (SWH) and the maximum wave height (H_{max}).

This paper investigates to what extent the improved description of ocean waves offered by the new instrument SWIM, as compared to SAR measurements, allows to account for a more detailed wave description as well as a posteriori analysis of large swell impacts on coral reefs and human assets. A precise description of the wave height under strong wind conditions is important to be able to investigate the impact on the coastal environment. Our study is focused on the Iles du Vent archipelago in French Polynesia (Moorea Island). We combine satellite and *in situ* measurements of ocean waves properties. These *in situ* measurements correspond to time series recorded by wave gauges deployed on the outer slope of coral reefs; they have so far only been used for the calibration-validation of SWIM (Hauser et al, 2021). Section 2 introduces the climatology of the ocean waves in the Moorea Island region and the associated expected limits of the SAR imagery. Section 3 is dedicated to the description of the database and of the collocation methods. Using both satellite and *in situ* data, we perform a statistical investigation of waves properties over the two years period from April 2019 to April 2021. We first investigate averaged properties (SWH parameters in Section 4) and then turn to the distribution of energy in the wave spectrum through a few detailed case studies (Section 5).

2 Wave Climatology and expected limits of the SAR observations in the region of the Iles du Vent archipelago

Using the numerical predictions of MFWAM, we investigated the climatology of ocean waves around the Iles du Vent archipelago, to which the Moorea and Tahiti islands belong, over a two-year period from April 2019 to April 2021.

The probability density function associated with the significant wave height is represented in Figure 1(a). Over this period, the MFWAM model indicates sea states ranging from slight to very rough sea states ($4 < SWH < 6$ m). Figure 1(b) highlights the dominant wavelength of ocean wave systems propagating around the Iles du Vent archipelago. The bimodal distribution corresponds to both the wind sea waves and short swells with wavelengths less than 150 m, and to swells with wavelengths comprised between 200 and 400 m. The latter correspond to swells generated by southern mid-latitude storms. This is highlighted in Figure 1(c), which shows the probability density function associated to the mean wave direction. Most of ocean wave energy comes from South, with directions comprised between approximately 100 and 220 degrees. Since

the azimuth direction of the Sentinel-1 SAR is about 13 degrees shifted from the South-North direction as it passes over this area, the SAR azimuth cut-off is thus expected to be a critical issue in this area of the world; most of ocean wave energy coming from directions very close to the azimuth direction of the Sentinel-1 SAR, and thus significantly altered by the afore mentioned cut-off.

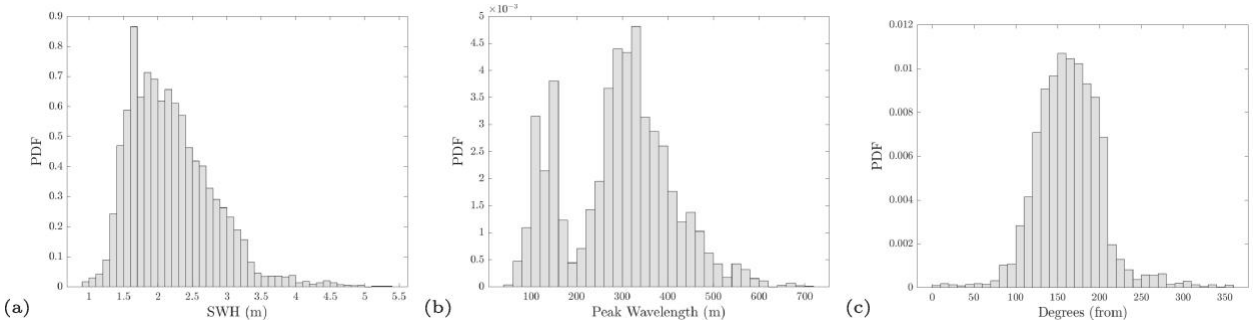

Figure 1. Climatology of (a) the significant wave height, (b) the peak wave length and (c) the mean wave direction ("from" convention) around the Iles du Vent archipelago. The probability density function (PDF) was computed from MFWAM model data between April 2019 and April 2021.

In order to investigate the consequences of the SAR azimuth cut-off issue, we used *in situ* measurements during Tropical Cyclone Oli in February 2010. These measurements were performed using a Seabird wave gauge (as part of the SNO-Corail network – http://observatoire.criobe.pf) deployed at 30 m depth on the outer slope of the Tiahura coral reef, northwest of Moorea Island. The eye of TC Oli came as close as 200 km from Moorea Island, but the wave gauge was deep enough not be destroyed by the TC. Figure 2 shows the sea wave height that we reconstructed from the pressure recording during TC Oli: the SWH reached 8.0 m and in the recording the maximum measured wave height was 9.8 m.

Then to mimic the spectral limitations of the SAR, the wave height was reconstructed after filtering out frequencies higher than the SAR cut-off value 0.1 Hz, which corresponds to a wavelength of the order of 150 m. This value is probably an underestimate, since it corresponds to intermediate surface winds, much lower than winds blowing in a tropical cyclone. Both the significant wave height and the maximum wave height are strongly affected by the spectral filtering: the SWH is divided by a factor 2, decreasing from 7.4 m to some 3.6 m as the cut-off filter is implemented, whereas the maximum wave height is divided by as much as 2.5, decreasing from 9.8 to 3.8 m. *In situ* observations show that the waves associated to TC Oli only became devastating to the ecosystem as well as infrastructure when the corresponding SWH reached 6 m, most of the material and ecological damage is associated with these high-amplitude waves which are very limited in time (a few hours). The underestimation of wave measurements due to instruments limitations such as the azimuth cut-off of SAR can thus have essential consequences on short term forecast as well as a posteriori damage analysis of wave impacts on coral reefs and human infrastructures.

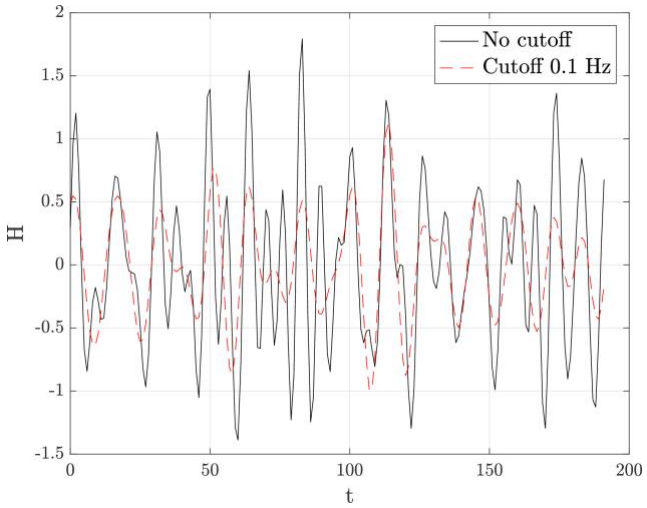

Figure 2. Time evolution of the ocean waves height h(t) reconstructed from a Seabird wave gauge recording during Tropical Cyclone Oli on 2010 February 4th at 10:46:01 UTC, performed on the outer slope of the Tiahura coral reef: (black) using the whole spectrum (SWH=8.0 m, H_{max}=9.8 m); (red) using a spectrum truncated above 0.1 Hz (SWH=3.6 m, H_{max}=3.8 m).

3 Data sets and collocation methods

3.1 Satellite observations

Our study extends from April 2019 to April 2021. We use the level 2 products of SWIM-CFOSAT (data reprocessed in version OP05-v5.1.2). The nadir-beam gives access to the SWH parameter among others, whereas the off-nadir rotating beams at 6°, 8° and 10° provide two-dimensional wave slope spectra. There is a consensus in the CFOSAT community to prefer the spectra measured by the beam at 10° (Hauser et al, 2021). Indeed, the radar cross-section observations at this incidence angle are the less sensitive to the wind effect and to speckle contamination. In their validation studies, Hauser et al (2021) and Liang et al (2021) among others have shown that they provide the best performances in terms of mean wave parameters compared to model or *in situ* data. This study is thus performed using the wave spectra estimated from the 10° beam observations. We recall here that wave spectra from SWIM are provided for wave cells (or boxes) of about 70 km x 90 km (along-track x across-track dimension) on each side of the nadir track. They are discretized in 12 propagation directions θ varying from 0° to 180° every 15° (with a 180° indetermination) and 32 wavenumbers k spanning from k_{min}=0.01 m^{-1} to k_{max}=0.28 m^{-1} with a width of wavenumber bin Dk such that Dk/k=0.1. The SWH is defined as

$$SWH = 4\, {E_{tot}}^{1/2}, \quad (1)$$

where E_{tot} is the total energy of the spectrum. It is calculated by converting the wave slope spectrum $F(k,\theta)$ to the wave height spectrum, $E(k,\theta)$, which corresponds to $F(k,\theta)/k^2$, and by integrating $E(k,\theta)$ as

$$E_{tot} = \iint E(k,\theta)\, k\, dk\, d\theta, \quad (2)$$

the double integration being performed over the directions θ and the wavenumbers k, between k_{min} and k_{max}.

We also use the SWH as measured by the altimetry mission Jason-3 SWH (1 Hz averaged) and the two-dimensional ocean wave height spectra of the level 2 product of the Sentinel 1a and 1b SAR wave mode (imagettes of 20 km x 20 km), discretized in 60 wavenumber bins in the range [0.01, 0.21] m^{-1} and 72 directions from 0° to 360°. This product also contains the SWH as provided by (1) and (2), as well as the shortest detectable wavelengths associated with the azimuth cut-off and the wave propagation directions.

3.2 *In situ* measurements

The Moorea Island has three coastlines which face to the north, southwest and southeast (Figure 3a). The island is encircled by a coral reef and a lagoon which is 500–700 m wide. In the frame of the Maeva project started in 2018, we installed two OSSI (Ocean Sensor System Inc) wave gauges on the external slope of the Tiahura coral reef (149.8998°W/17.4823°S) at 12 m and 30 m depth respectively. A third wave gauge was placed at 30 m depth on the Paroa coral reef (149.8187°W/17.6078°S) (Figure 3). These wave gauges record continuously the pressure at 1 Hz; their autonomy is 6 months. These temporal recordings correspond to very rare *in situ* measurements in coral reef environments and can be used to estimate time series of ocean surface waves elevation. Unlike the continental floor characterized by gentle slopes, the volcanic islands such as Moorea are characterized by steep slopes. The ocean waves are thus hardly affected by the bottom effects and the dispersion relationship remains that known as "deep water" while approaching the reef.

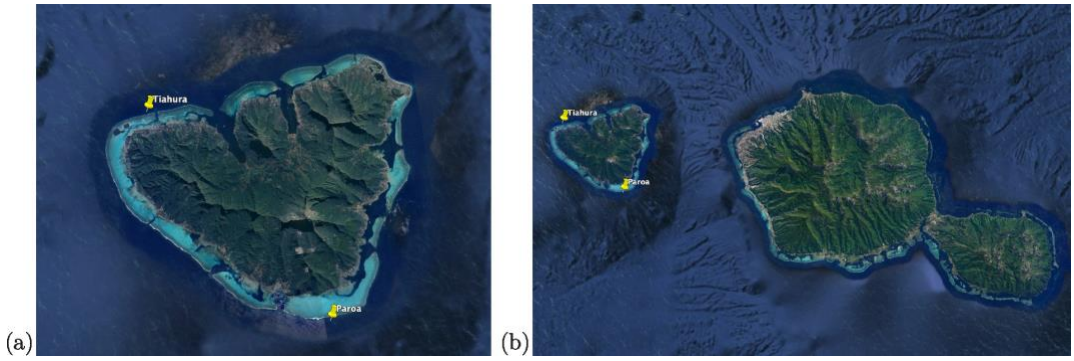

Figure 3. (a) The Moorea Island, located in the South Pacific Ocean between 17.4714° and 17.6058° south and 149.7522° and 149.9269° west. (b) The Tahiti Island lies 20 km south-east of Moorea. The two sites where OSSI wave gauges have been installed in the frame of the Maeva project are highlighted in yellow.

For this study, we use the two OSSI wave gauges installed at 30 m depth. From the continuous 1Hz pressure recording provided by each wave gauge, we reconstructed time series of elevation and from that omni-directional spectra of ocean surface waves (Bonneton & Lannes, 2017). The main steps of the post-processing are the following ones. Each signal is periodized using a Tukey (tapered cosine) window (Bloomfield, 2000). An average over 30 signals, each 4 minutes long, starting every 2 minutes (thus over a total duration of one hour) is performed to reduce the background noise. The thus-obtained omni-directional frequency spectrum, $E_f(f)$, is converted in wavenumber spectrum $E_k(k)$ using the gravity waves dispersion relation. The attenuation of waves with depth is then corrected for. The attenuation prevents us from measuring the high frequency waves which are the most severely damped: the cut-off frequency in OSSI

measurements at 30 m is 0.2 Hz, which corresponds to a wavelength of about 40 m. The total energy is calculated by integrating E_k(k) over k as

$$E_{tot} = \int E_k(k)dk. \quad (3)$$

The pressure measurement by each wave gauge does not provide any information on wave directions. Nevertheless, the comparison of the signals measured by the two wave gauges, which strongly depend on wave directions, provides useful validation for the wave directions. On the one hand, the wave gauge located on the Paroa coral reef measures the energy coming roughly from the range [130°, 270°] (0° meaning from North and 270° from West). Without the masking by the Tahiti Island, it would measure over a wider range [90°, 270°], being affected only by the Moorea Island masking. On the other hand, the Tiahura wave gauge is mainly affected by the masking by the Moorea Island and measures energy roughly coming from the range [270°, 70°]. The sum of the energy measured by both wave gauges thus gives access to the waves coming from the range [130°, 70°]. Such a sum may raise the question of overlap, especially concerning the energy coming from West (270°) which is detected by both wave gauges. However, Figure 1(c) shows that in climatological average, there is a minor fraction of energy coming from the West around the Iles du Vent archipelago. Thanks to the geographical distribution of wave gauges around the Moorea Island, the *in situ* energy of waves can be retrieved by summing the energy measured by both wave gauges; the SWH is then derived using (1). In the following, the omnidirectional spectra and wave parameters thus obtained are labelled as *in situ.* Because of the masking by the Tahiti Island, only the wave energy coming from the range [70°,130°] cannot be detected by the wave gauges.

3.3 Collocation method

Between the 20th of April 2019 and the 10th of April 2021, we identified 324 ground tracks of CFOSAT at less than 300 km from the Moorea Island. This corresponds to 2080 geographical boxes of size 70 x 90 km² located within 300 km around Moorea (Figure 4). The passage of the satellite over this region occurs between 5 and 6 am UTC and between 4 and 5 pm UTC. The SAR of Sentinel 1 passes over French Polynesia about one hour earlier: the time-lapse between SWIM and SAR data is thus lower than one hour. Over the period of interest, 159 SAR passages occurred within 300 km around Moorea less than one hour from a SWIM pass. We also performed a collocation of SWIM and the Jason-3 altimeter: we selected 236 colocalized data by allowing a maximum distance of 300 km between the SWIM boxes and the altimeter measurement, and a maximum time-lapse of 3 hours.

Due to power supply issues, the pressure records by wave gauges do not fully cover the period of interest: a few days may indeed elapse between the end of recording and the change of battery. There are 247 (resp. 220) passages of SWIM during which the Paroa (resp. Tiahura) wave gauge was recording the pressure, and we identified 209 SWIM passages during which both wave gauges were operational. Because of the post-processing involving 30 signals over a total period of one hour, the time-lapse between SWIM and wave gauges measurements is equal to 30 minutes, by construction.

The results shown in this paper correspond to a maximum collocation distance of 300 km. Such a value is larger than the values usually used for this type of study, which are of the order of a few tens of kilometers. This choice was made to get a number of collocated points sufficiently large to get meaningful statistics. Using smaller values for the maximum distance does not alter significantly our results, which indicates a certain homogeneity of waves properties within a few hundred kilometers around the Moorea Island (see also section 5).

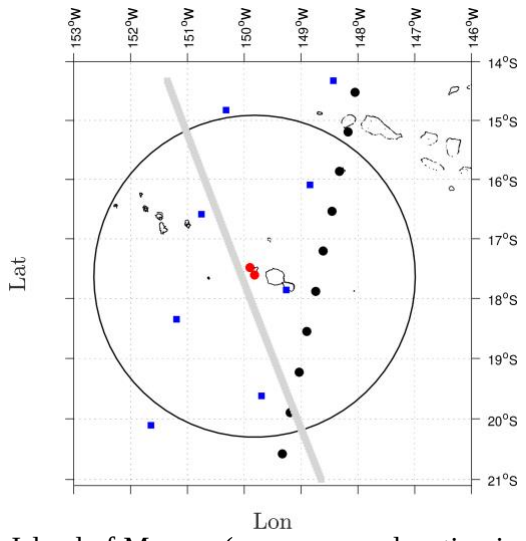

Figure 4. Map centered on the Island of Moorea (wave gauges location in red). The black thin circle line indicates a 300 km distance from Moorea. Black dots: mean position of the SWIM L2 products on 06 May 2019 between 16:49:29 and 16:51:06. Blue squares: position of the SAR S1 imagettes on the same day between 15:35:32 and 15:37:44. In gray: ground track of the Jason-3 ku-band radar the same day between 16:22:51 and 16:25:09.

4 Statistical study of the significant wave height

First, we focus on the significant wave height measured by satellite instruments around the Iles du Vent archipelago. We start with a comparison between SWIM and the altimeter of Jason 3. For each of the 2080 boxes of SWIM we identified within a 300 km distance of Moorea, we searched for the nearest SWH measurement by the Ku-band radar of Jason 3, we thus obtained 236 colocalized data. Figure 5 highlights that in this region, the SWH provided by the nadir beam of SWIM compares very well with the SWH measured by Jason 3. This result is consistent with recent studies (Hauser et al, 2021; Liang et al, 2021) which assess the good performance carried out at the global scale of the nadir beam of SWIM by comparison to existing altimeters.

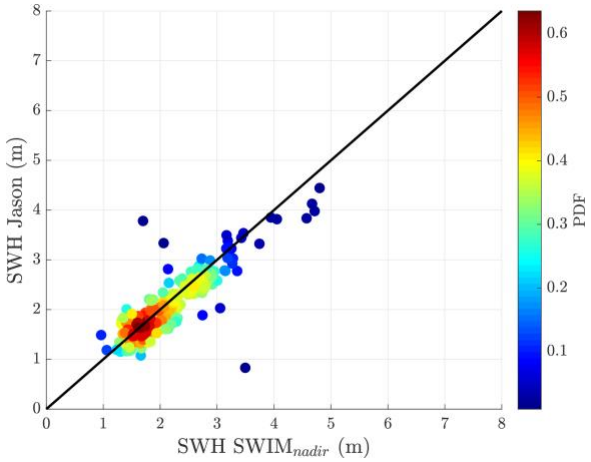

Figure 5. SWH as measured by the Ku-band radar of Jason 3 as a function of the SWH measured by SWIM (nadir-beam) around the Moorea Island. Probability density function (in colors) constructed with 236 colocalized data (maximum distance: 300 km, maximum time-lapse: 3 hours). Black line: y=x line. (Bias: -0.02; RMSE=0.74.)

The comparison between SWIM and the SAR of Sentinel 1 can first be performed using the SWH from the 2D spectra as provided by (1) combined with (2). We compared 159 collocated SWIM and SAR measurements, corresponding to the nearest SWIM box and SAR imagette from the Moorea Island, separated in time by less than one hour. Figure 6(a) compares the SWH measured by SAR with that measured by the SWIM beam 10°. The SAR detects less energy than SWIM, and the difference increases with SWH. To investigate such a difference, we constructed two partitions: the first one corresponds to the energy associated to wave numbers smaller than $k^*=0.04$ m^{-1}, denoted as E_1, whereas the second one corresponds to the remaining spectrum (energy E_2). In other words, the calculation of E_1 (resp. E_2) is performed using (2) with integration limits varying from k_{min} to k^* (resp. from k^* to k_{max}). In Figures 6(b) and 6(c), we plotted the quantities $4\sqrt{E_1}$ and $4\sqrt{E_2}$. These two graphs show that the underestimation of the SWH by the SAR originates from wavenumbers larger than 0.04 m^{-1}: the SAR underestimates the energy of wavelengths smaller than about 150m. This is the signature of the azimuth cut-off inherent to SAR which limits wind-sea measurements as discussed above. This effect is indeed highlighted in Figure 7 which relies on the dominant wave propagation directions (mean primary swell wave directions) as modelled by MFWAM. These directions have been extracted from the MFWAM 2D spectra colocalized with the SWIM data used in the comparison shown in Figure 6. Figure 7(a) shows that in most cases, the dominant wave direction relative to the SAR azimuth, $\Delta\theta$, is small enough so that its cosine is close to unity. In other words, the dominant waves do propagate in directions close to the SAR azimuth direction. To further quantify the cut-off undergone by the waves as measured by the SAR, the shortest detectable wavelength in the dominant direction, $\lambda_{c,\Delta\theta}$, can be compared to the azimuth cut-off wavelength λ_c. The comparison is shown in Figure 7(b). As expected, $\lambda_{c,\Delta\theta}$ is very close to λ_c in most cases: this result is consistent with the fact that the dominant waves come from the South (see figure 1c) and thus propagate in a direction close to the SAR azimuth. Figure 7(b) also shows that the most probable shortest detectable wavelength during the period of investigation is between 150 and 200 m. These results corroborate the underestimation of the SAR significant wave heights compared to SWIM (Figure 6(a) and 6(c)) .

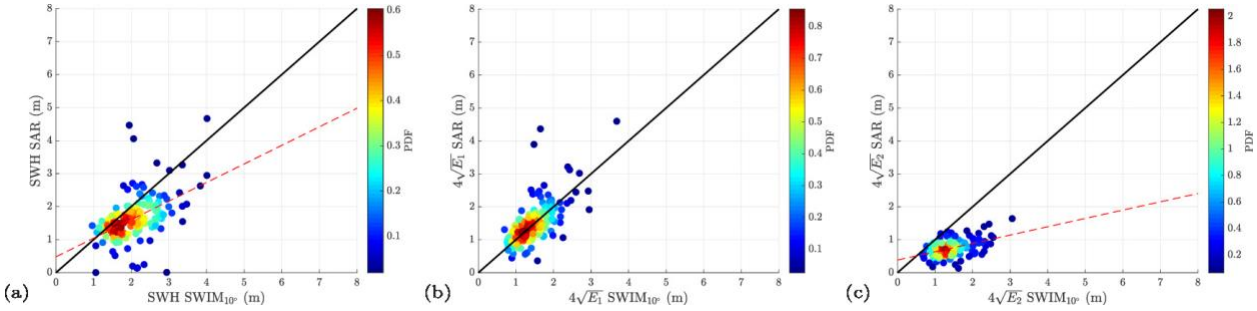

Figure 6. Scatterplot and probability density function (in colors) associated to 159 collocated wave measurements by SAR (in ordinate) and SWIM beam 10° (in abscissa). (a) SWH; (b) $4\sqrt{E_1}$; (c) $4\sqrt{E_2}$, where E_1 (resp. E_2) is the spectrum energy restricted to k<0.04 m^{-1} (resp. k>0.04 m^{-1}). Red curve on (a) and (c): linear fit of data. Black line: y=x line. (Bias: (a) -0.43 (b) 0.03 (c) -0.68; RMSE: (a) 0.78 (b) 0.49 (c) 0.78.)

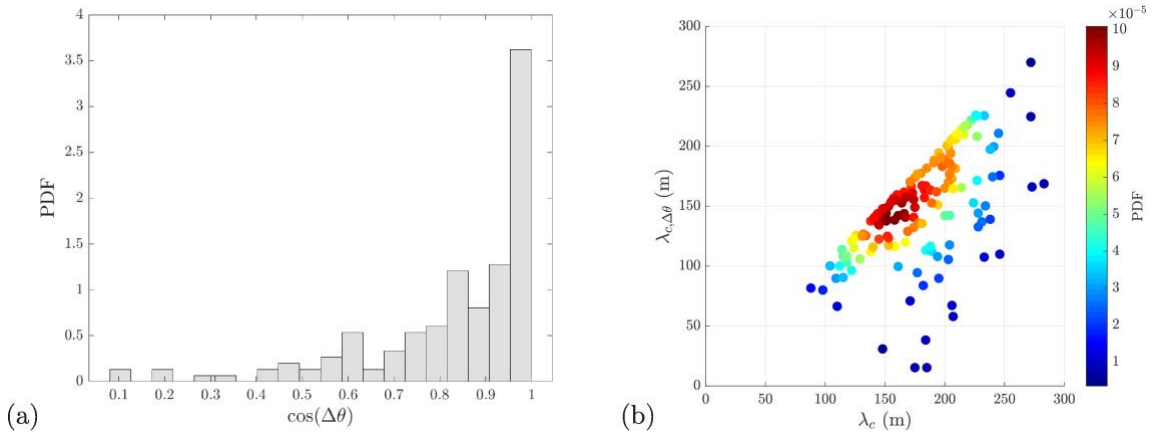

Figure 7. (a) Probability density function of cos(Δθ), Δθ being the angle between the primary swell wave mean direction (as modelled by MFWAM) and the SAR azimuth direction. (b) Scatterplot and probability density function (in colors) of the shortest detectable wavelength in the dominant direction as a function of the azimuth cut-off wavelength.

The comparison between SWIM and the *in situ* wave gauges was performed using 209 collocated data. Figure 8(a) shows the SWH measured by the SWIM beam 10° and the SWH reconstructed from the *in situ* measurements by both wave gauges. The former measurement is slightly larger than the latter, in other words SWIM detects more energy than the wave gauges. This bias may be due to the masking by the island of Tahiti, which prevents the wave gauges from measuring the wave energy coming from the angular sector [70°,130°]. To overcome this bias, an angular mask was applied to SWIM 2D spectra dropping the energy in the 4 bins between 75° and 135°. The SWH obtained after this masking of the SWIM 2D spectra is shown in Figure 8(b): this modified quantity appears fully consistent with the SWH measured by wave gauges. However, the 2D spectra of SWIM have a 180° ambiguity, which means that the angular sector [255°,315°] must also be masked in SWIM spectra; one might thus have expected a modified SWH slightly smaller than the *in situ* measurements, even if the climatology study, shown in Figure 1(c), suggests that there is little energy coming from those directions. Hence, the possibility of an additional bias leading to a slight overestimation of the wave energy measured by SWIM cannot be excluded at this stage; a deeper investigation can however be performed.

For an appropriate comparison, the angular mask aiming at mimicking the masking of wave gauges by the Tahiti Island is applied to the SWIM 2D spectra. The spectral partitioning around the wavenumber 0.04 m^{-1}, described above, is applied to the masked SWIM spectra and to the *in situ* omni-directional spectra. Figure 9 compares the resulting quantities $4\sqrt{E_1}$ (panel a) and $4\sqrt{E_2}$ (panel b). Figure 9(b) shows that contrary to the SAR, the SWIM beam 10° does not underestimate the energy associated with wavenumbers larger than 0.04 m^{-1}. We can however notice a slight overestimation of the spectral energy corresponding to smaller values of wavenumber, compared to the *in situ* measurements (the bias in Figure 9(a) is indeed slightly negative).

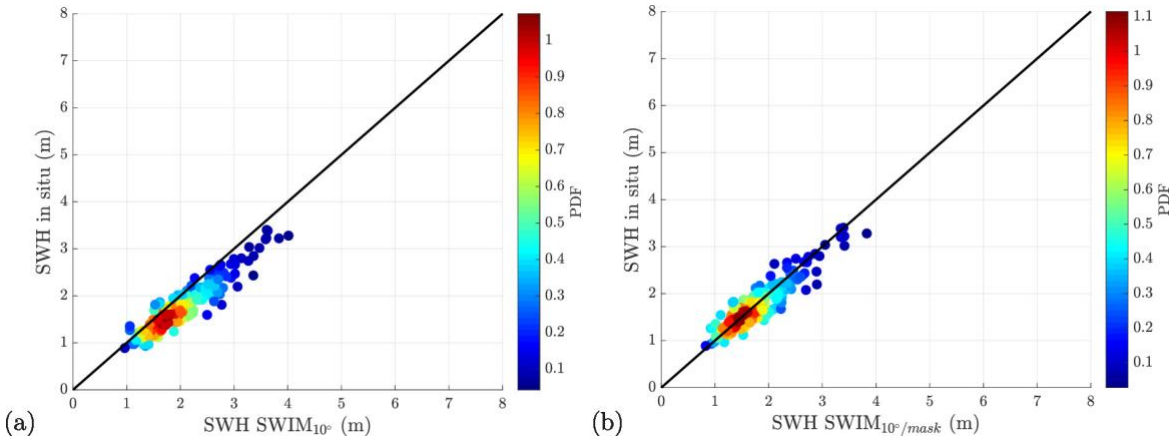

Figure 8. (a) SWH as measured by wave gauges as a function of SWH measured by SWIM beam 10°. (b) Same as (a) except that an angular mask between 75° and 135° was applied to SWIM 2D spectra before computing the SWH. Scatterplot involving 209 collocated data. In colors: probability density function. Black line: y=x line. (Bias: (a) -0.28 (b) -0.03; RMSE: (a) 0.35 (b) 0.21.)

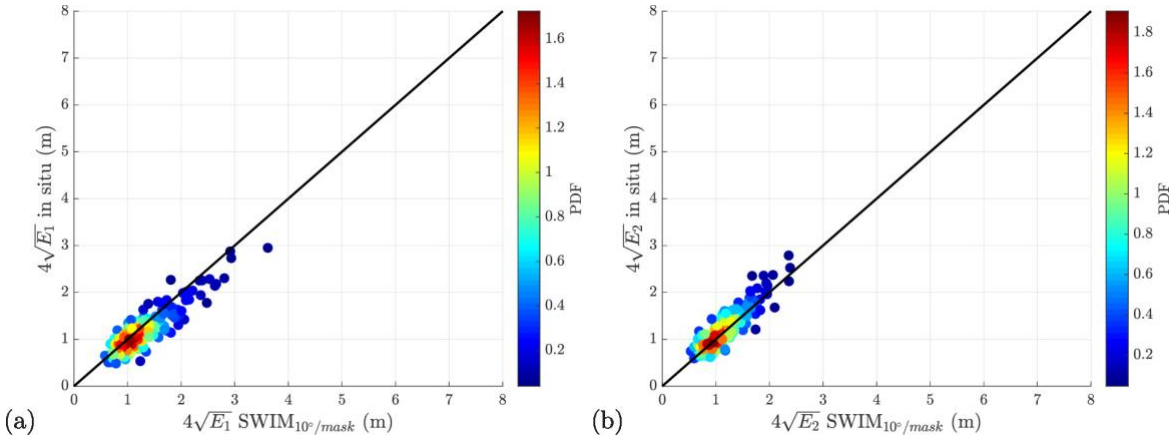

Figure 9. Scatterplot and probability density function (in colors) associated to 209 collocated wave measurements by wave gauges (in ordinate) and by SWIM beam 10° (in abscissa). (a) $4\sqrt{E_1}$; (b) $4\sqrt{E_2}$, where E_1 (resp. E_2) is the spectrum energy restricted to k<0.04 m^{-1} (resp. k>0.04 m^{-1}). Black line: y=x line. (Bias: (a) -0.13 (b) 0.06; RMSE: (a) 0.25 (b) 0.19.)

5 Spectral energy distribution

Having performed a statistical analysis on the significant wave height and partitions, we will now turn in this section to a more detailed analysis of the full wave spectra, beyond the above analysis which relied on integral quantities.

5.1 Dominant wavelength

The spectral energy repartition can first be characterized by the peak wavelength. The SWIM L2 product provides a wave parameter denoted as “dominant wavelength”, defined as the wavenumber weighted by the energy around the two third of the maximum energy of the peak in the 2D wave slope spectrum. It roughly corresponds to a smoothed estimation of the peak wavelength in the 2D wave slope spectrum (see Hauser et al, 2017). However, the *in situ* spectra

correspond to wave height omnidirectional spectra. For comparisons to make sense, we estimated the SWIM peak wavelength by computing the azimuthally integrated wave height spectrum, E_k(k). Figure 10 compares the peak wavenumber as measured by the wave gauges and by SWIM. Both values are generally consistent, thus highlighting that the agreement goes beyond the SWH estimation. There are however a few cases for which the SWIM peak wavenumber is strongly underestimated. This is a known artefact of the SWIM wave height spectra, which exhibit a parasitic peak at low wavenumber because of the amplification of a low energy floor at small wavenumbers when converting wave slope spectra to wave height spectra. These outliers are mainly observed in cases of low significant wave heights.

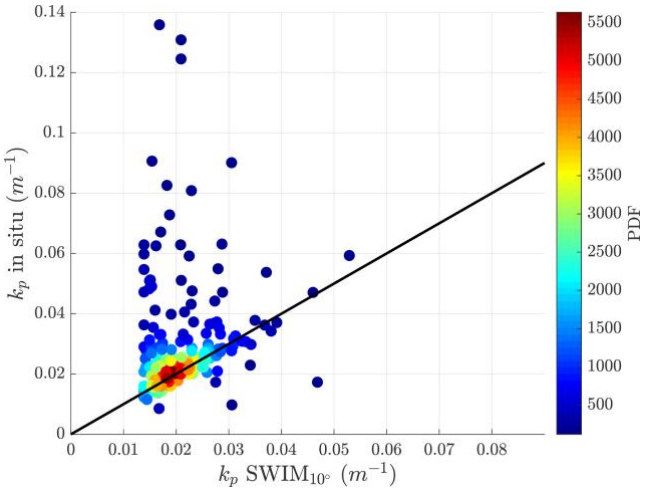

Figure 10. Scatterplot and probability density function (in colors) associated to 209 collocated wave measurements by wave gauges (in ordinate) and by SWIM beam 10°, corresponding to the peak wavenumber estimated from the wave height omnidirectional spectra. (Bias: 0.01; RMSE: 0.02.)

5.2 Case studies

A more detailed investigation is now undertaken through 4 case studies during spring 2020. These cases have been selected to highlight how the satellite performances in measuring the wave properties depend on the sea-state.

Figure 11(b,d,f,h) shows omni-directional wave height spectra, E_k(k), deduced from SWIM, SAR and *in situ* measurements for each of these 4 cases; Figure 11(a,c,e,g) shows the corresponding locations. Instead of limiting ourselves to the spectra closest to the wave gauges, we also plotted the mean spectra over the SWIM boxes and over the SAR imagettes located within 300 km around Moorea, in order to highlight the weak spatial variability of wave properties around the Iles du Vent archipelago. The resulting mean spectra are shown in dashed. The nearest spectra and the mean spectra do not vary significantly with location. This is a general observation in this area; the relative homogeneity of waves properties within a few hundred kilometers around the Moorea Island justifies the collocation criteria described in section 3.

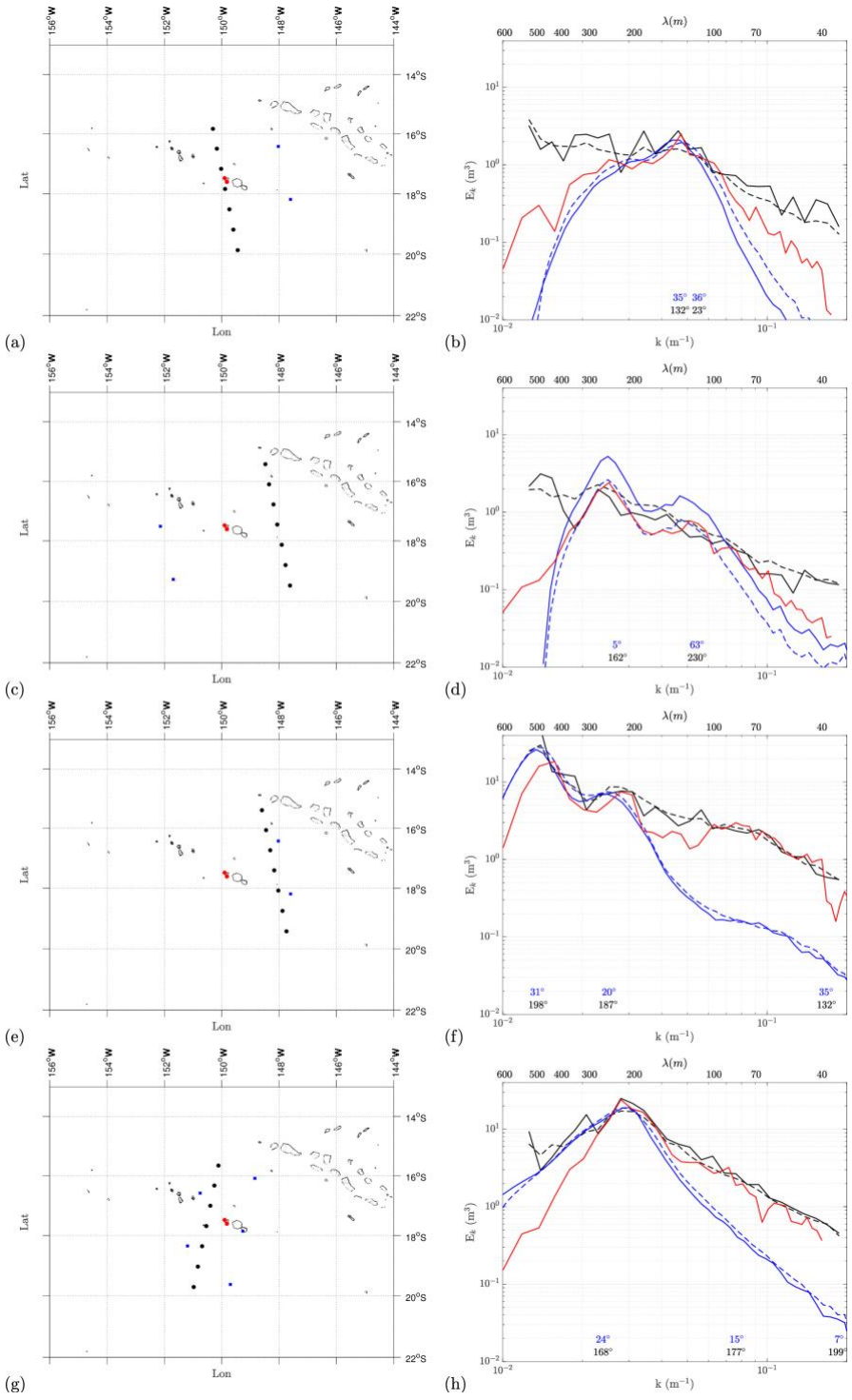

Figure 11. (a,b) Case A: March 11, 2020; (c,d) Case B: April 13, 2020; (e,f) Case C: May 22, 2020; (g,h) Case D: June 5, 2020. (a,c,e,g) Maps showing the locations of wave gauges (in red), SWIM boxes (in black) and Sentinel1-SAR imagettes (in blue). (b,d,f,h) Omnidirectional wave height spectra in log-log scale as measured by the wave gauges (in red), the SAR (in blue) and SWIM (in black). Solid lines: spectra of the nearest SWIM box (black) and SAR imagette (blue) to Moorea; Dashed lines: mean spectra over the 7 SWIM boxes (black) and over the SAR imagettes (blue) within 300 km around Moorea, as shown on (a,c,e,g). The horizontal axis indicates the wavenumber (bottom) and the wavelength (top). The wave propagation direction of each MFWAM partition is indicated in black above the bottom horizontal axis. The angle between this direction and the SAR azimuth direction ($\Delta\theta$) is indicated in blue.

The first two cases (denoted as A and B) shown in Figure 11(a,b,c,d) correspond to moderate waves, the SWH being smaller than 1.5 m. The most striking point in both cases is that the SWIM spectra are quite flat compared to the spectra provided by the SAR and the wave gauges, which both exhibit more marked variations. The performance of SWIM in characterizing moderate sea states is not as good as that of the SAR. This is probably due to the limitation of SWIM measurements in low sea-state conditions, where speckle noise is not perfectly eliminated and may induce a parasitic peak at small wavenumbers and an increase in the noise floor at large wave numbers (Hauser et al, 2021).

The two other cases, cases C and D, shown in Figure 11 (e,f,g,h) correspond to rough sea states with a SWH of 3 m. Case C was obtained on May 22, 2020, when a moderate wind of 10 m/s blew for several hours over the French Polynesia, whereas case D corresponds to June 5, 2020, when the archipelago was swept by winds of 6 m/s associated to a depression located South of Moorea. The spectra shown in Figure 10(f) exhibit two peaks corresponding to southern swells of 200 and 400 m; those in Figure 10(h) exhibit a peak associated to a swell of 200 m. These peaks are captured by the wave gauges, the SAR and SWIM. The wave gauges and SWIM detect more energy for $k>0.04$ m^{-1} in cases C and D than in cases A and B. This is however not the case for the SAR whose spectra decrease much more rapidly with k than the *in situ* and SWIM spectra in cases A, C and D. Hence, in cases C (resp. D), the SWH measured by the SAR is 2.0 m (resp. 2.4 m) whereas the wave gauges and SWIM estimate the SWH to be 3 m. This is due to the azimuth cut-off. As explained in section 4, the dominant swell, generally comes from the South in this area, i.e. is close to the azimuth direction. This is indeed the case for both of these examples, as shown in Figures 11(b,d,f,h) where the directions of each partition modelled by MFWAM are indicated above the horizontal axis, as well as the angle $\Delta\theta$ which measures the difference between the waves propagation direction and the azimuth. This highlights that the drops in SAR spectra correspond to small values of $\Delta\theta$ (cases A,C and D), whereas situations corresponding to a larger value of $\Delta\theta$ (63° in case B) do not yield such a bias.

Figure 12 presents the full directional spectra corresponding to case D as measured by SWIM (panel (a)) by the SAR (panel (b)) and as modelled by MFWAM (panel (c)). This illustrates the advantages and limitations of both instruments. The 180° indetermination of SWIM is evident on panel (a), as are the parasitic peaks at small wavenumbers on the wave height spectra. The cut-off effect of the SAR on the dominant waves coming from the South (close to the azimuth direction) is also clearly highlighted. The MFWAM directional spectrum is also provided for comparison (panel (c)).

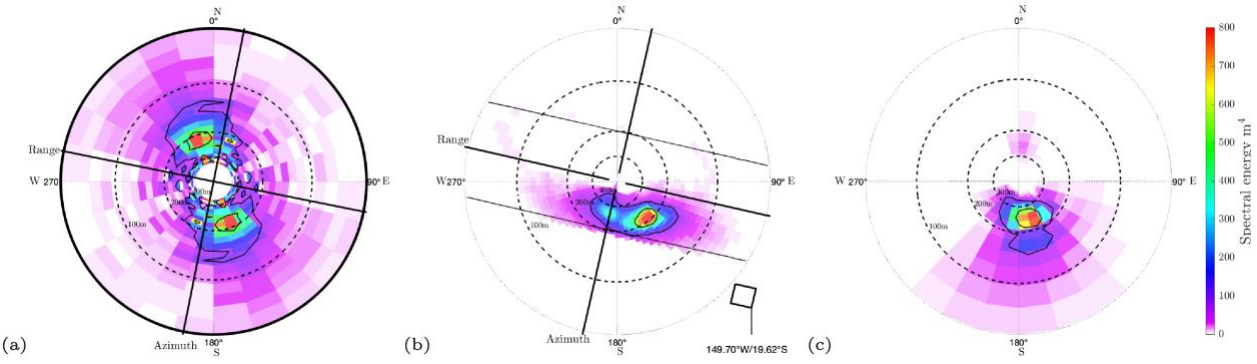

Figure 12. Two-dimensional wave height spectra associated with the case D shown in figure 11(g-h) and relying on (a) the SWIM box nearest to Moorea (here using the combined spectrum), (b) the nearest SAR imagette and (c) the colocalized MFWAM model. In (a) and (b) the directions of azimuth and range are indicated as solid lines. In (b), the shortest detectable wavelengths are indicated by the thin solid lines.

6 Conclusions

In this paper we investigated to what extent the real-aperture radar SWIM on-board CFOSAT allows to document the ocean surface waves in conditions of the South Pacific coral reef environments and compare the SWIM performance to *in situ* and SAR (Sentinel-1) observations.

Comparing *in situ* and satellite measurements around the Moorea Island, we have shown that in rough sea states, SWIM wave measurements offer a chance to measure the wind-sea, corresponding to wavelengths smaller than about 150 m, whereas the SAR is limited by the azimuth cut-off, which prevents measurements of the wind sea waves or short swell. This limitation is particularly important in this region where most of the wave energy comes from the South and propagates in directions close to the SAR azimuth direction (the SAR can measure wavelengths up to 30 m for waves propagating in directions orthogonal to the azimuth). These wavelengths have been shown to be important to properly estimate the SWH from SAR spectra under strong wind conditions, a decisive point to investigate the impact of extreme weather conditions on tropical islands.

It should however be noted that for low to moderate sea states, the SAR appears to provide more reliable measurements than SWIM, due to remaining speckle contamination in the SWIM spectra. Hence, the complementarity of the SWIM and SAR measurements in the South Pacific strongly depends on the wavelength, the significant wave height and the direction of propagation. In this region, and for moderate to high sea-state conditions, the real-aperture radar technology appears to open the possibility of a finer estimate of waves impact and potential damages.

A precise description of the large amplitude waves generated by extreme meteorological events is essential in a context of global warming and sea level rise, as the coral reefs shelter both the inhabitants and the infrastructures from devastating ocean waves. In the case of tropical cyclone Oli (2010) the most devastating waves, with SWH above 6 m, only lasted a few hours. An accurate satellite description of these waves requires a reconstruction of the wave spectrum in the range 70-500 m recently made available via the rotating radar technology.

Acknowledgments

This study was carried out in the frame of the Maeva project, funded by the CNES/TOSCA. We thank the CRIOBE, in particular Y. Chancerelle, F. Zuberer, G. Siu, G. Iwankov and F. Lerouvreur for their logistic support and help in installing and recovering the wave gauges.

References

Aouf, L., Hauser, D., Chapron, B., Toffoli, A., Tourain, C., & Peureux, C. (2021). New directional wave satellite observations: Towards improved wave forecasts and climate description in Southern Ocean. *Geophysical Research Letters*, 48, e2020GL091187. doi:10.1029/2020GL091187

Alpers, W. R., & Brüning, C. (1986). On the relative importance of motion-related contributions to the SAR imaging mechanism of ocean surface waves. *IEEE Trans. On Geosci. and Rem. Sens., 24*, 873–885. doi:10.1109/TGRS.1986.289702

Beck, M.W., Losada, I. J., Menéndez, P., Reguero, B. G., Díaz-Simal, P., & Fernández, F. (2018). The global flood protection savings provided by coral reefs. *Nat. Com.*, 9, 2186. doi: 10.1038/s41467-018-04568-z.

Bonneton, P., & Lannes, D. (2017). Recovering water wave elevation from pressure measurements. *J. Fluid Mech., 833*, 399-429. doi:10.1017/jfm.2017.666

Bishop, C. T., & Donelan, M. A. (1987). Measuring waves with pressure transducers. *Coast. Eng., 11 (4)*, 309–328. doi:10.1016/0378-3839(87)90031-7

Bloomfield, P. (2000). Fourier Analysis of Time Series: An Introduction. New York: John Wiley.

Booij N., Ris R. C., & Holthuijsen L. H. (1999). A third-generation wave model for coastal regions, part 1: Model description and validation. *Journal of Geophysical Research, 104(C4)*, 7649-7666. doi:10.1029/98JC02622

Cavaleri, L., Alves, J.-H., Ardhuin, F., Babanin, A., Banner, M., Belibassakis, K., et al. (2007). Wave modelling–the state of the art. *Prog. Oceanogr., 75 (4)*, 603–674. doi:10.1016/j.pocean.2007.05.005

Cinner, J. E., Maire, E., Huchery, C., MacNeil, M. A., Graham N. A. J, Mora, C., et al (2018). Gravity of human impacts mediates coral reef conservation gains. *Proceedings of the National Academy of Sciences, 11*, E6116-E6125. doi: 10.1073/pnas.1708001115.

Hasselmann, K., Chapron, B., Aouf, L., Ardhuin, F., Collard, F., Engen, G., et al. (2012). The ERS SAR Wave Mode – A breakthrough in global ocean wave observations. (Vol.1326, pp. 167–197). *European Space Agency, (Special Publication) ESA SP*.

Hauser, D., Tison, C., Amiot, T., Delaye, L., Corcoral, N., & Castillan, P. (2017). SWIM: The first spaceborne wave scatterometer. *IEEE Trans. Geosci. Remote Sens., 55, 5*, 3000–3014. doi:10.1109/TGRS.2017.2658672

Hauser, D., Tourain, C., Hermozo, L., Alraddawi, D., Aouf, L., Chapron, B., et al (2021). New observations from the SWIM radar on board CFOSAT: instrument validation and ocean wave measurement assessment, *IEEE TGARS, 1,* 05-26. doi:10.1109/TGRS.2020.2994372

Hoegh-Guldberg, O., Pendleton, L. & Kaup, A. (2019). People and the changing nature of coral reefs. *Reg. Stu. Mar. Sci., 30,* 100699. doi:10.1016/j.rsma.2019.100699

Kerbaol, V., Chapron, B., & Vachon, P. W. (1998). Analysis of ERS-1/2 SAR Wave Mode Imagettes. *J. Geophys. Res., 103(C4),* 7833-7846. doi:10.1029/97JC01579

Kuleshov, Y., Qi, L., Fawcett, R., & Jones, D. (2008). On tropical cyclone activity in the Southern Hemisphere: trends and the ENSO connection. *Geophys. Res. Lett.,* 35:L14S08. doi:10.1029/2007GL032983

Liang, G., Yang, J., & Wang, J. (2021). Accuracy Evaluation of CFOSAT SWIM L2 Products Based on NDBC Buoy and Jason-3 Altimeter Data. *Remote Sens.,* 13, 887. doi:10.3390/rs13050887

Ribal, A., & Young, I. R. (2019). 33 years of globally calibrated wave height and wind speed data based on altimeter observations. *Sci Data., 6(1),* 77. doi:10.1038/s41597-019-0083-9

Tolman H. L. (1998). Validation of a new global wave forecast system at NCEP. In: Edge BL, Helmsley JM, editors. Ocean Wave Measurements and Analysis. Virginia Beach, VA, USA: ASCE; pp. 777-786

WAMDI Group (1988). The WAM model – A third-generation ocean wave prediction model. *Journal of Physical Oceanography,18,* 1775-1810. doi:10.1175/1520-0485(1998)018